Electronic Supplementary Material (ESI) for Journal of Materials Chemistry A.

Supporting Information

Designing a Schottky coupled p-n junction to enhance the kinetic behavior of the oxygen evolution reaction

Guangping Yang[a], Sining Yun[a, *], Tianxiang Yang[a], Jiaoe Dang[a], Yongwei Zhang[a] and Zhiguo Wang[a]

[a]Functional Materials Laboratory (FML), School of Materials Science and Engineering, Xi'an University of Architecture and Technology, Xi'an, Shaanxi, 710055, China.

* Corresponding author: Prof. Sining Yun
E-mail: alexsyun1974@aliyun.com; yunsining@xauat.edu.cn

Materials characterizations

The morphology of the samples was checked by scanning electron microscopy (SEM, ZEISS G500, Germany). The microstructure and HAADF-STEM images of the fabricated catalysts were analyzed by transmission electron microscopy (TEM, FEI TECNAI F20, America). The phase structure and chemical states were recorded by powder X-ray diffractometer (XRD, MDI D/Max 2200, Japan) and X-ray photoelectron spectroscope (XPS, THERMO ESCALAB 250XI, America). The XPS were recorded on a K-alpha apparatus (Thermo Scientific) equipped with a monochromatic Al Kα source (hν = 1486.6 eV). The reference scale was calibrated by adjusting the C-H component of the adventitious carbon to 284.8 eV. The XPS spectra were analyzed by using Avantage software. The ultraviolet-visible spectrophotometer (UV-vis, UV-3600i Plus, Japan) with barium sulfate as the reference and ultraviolet photoemission spectroscopy (UPS, PHI5000 Versa Probe III, Japan) were acquired to determine the energy level diagram. Raman spectra were conducted with a 532 nm excitation laser on a Raman spectrometer (LABRAM HR Evolution, France). The Raman spectrometer was used for in-situ Raman measurements together with a three-electrode system equipped with an electrolytic cell. The solid-liquid contact angle was tested on a goniometer (JC2000DM, China) to evaluate the hydrophilicity of heterojunction catalysts.

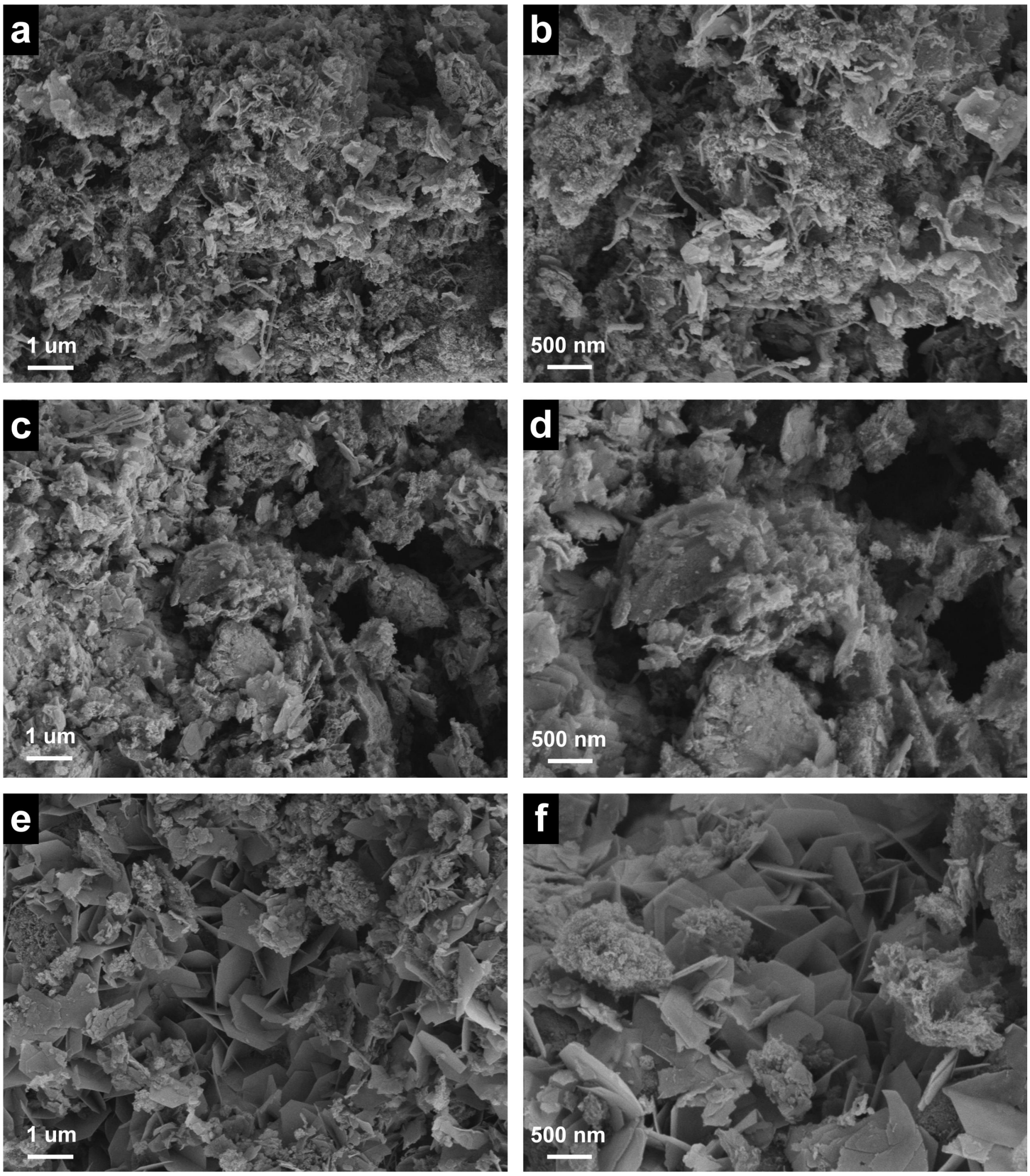

Fig. S1. SEM images of Fe_3C-NG@NiFe at different hydrothermal reaction times. (a-b) 3, (c-d) 6, (e-f) 9 hours.

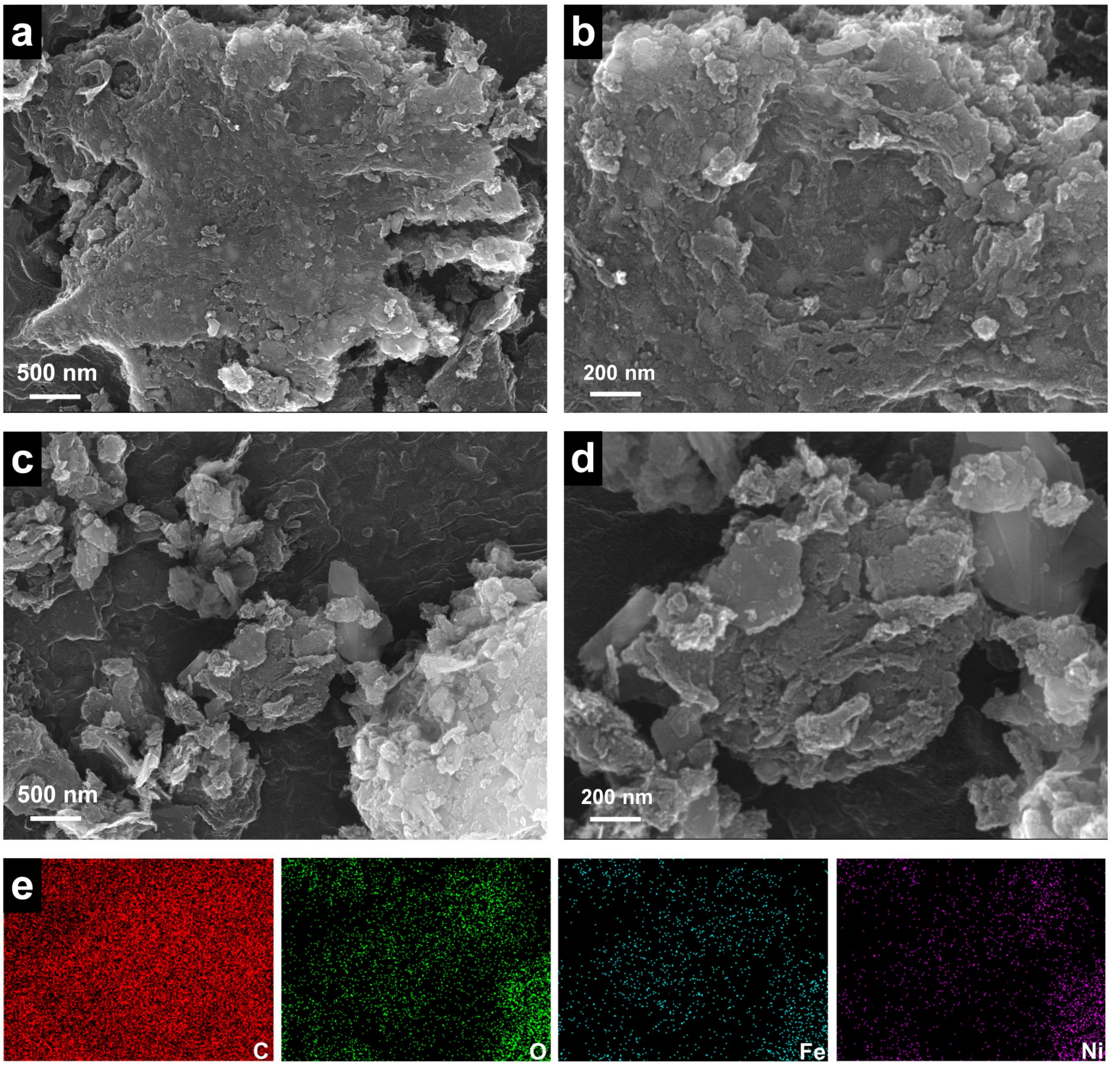

Fig. S2. Structure characterizations of the Fe_3C and Fe_3C@NiFe catalysts. SEM images of (a-b) Fe_3C and (c-d) Fe_3C@NiFe with different magnifications. (e) The corresponding EDS mapping of Fe_3C@NiFe.

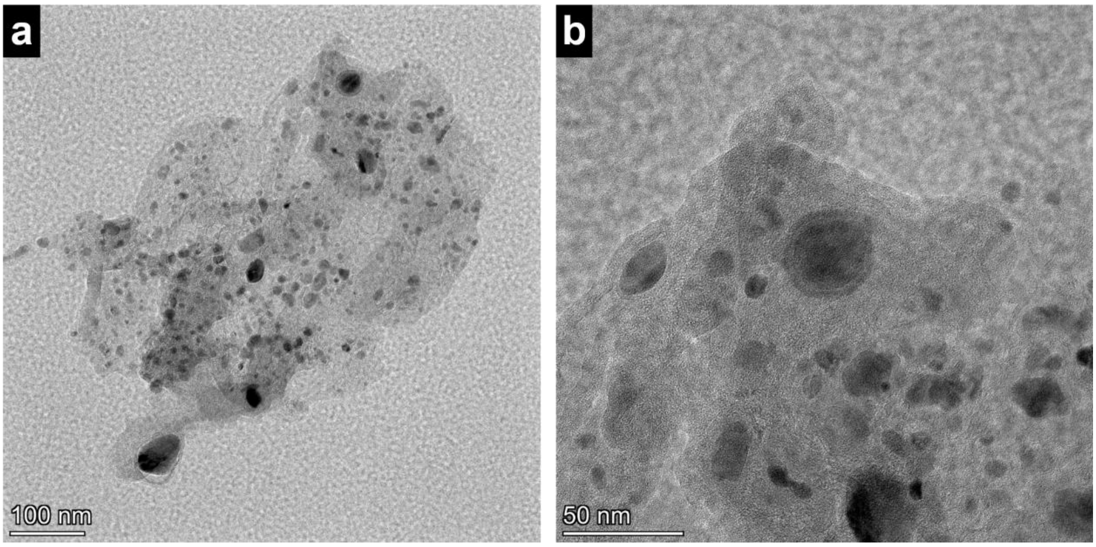

Fig. S3. Structure characterizations of the Fe_3C-NG catalysts. (a-b) TEM images of Fe_3C-NG with different magnifications.

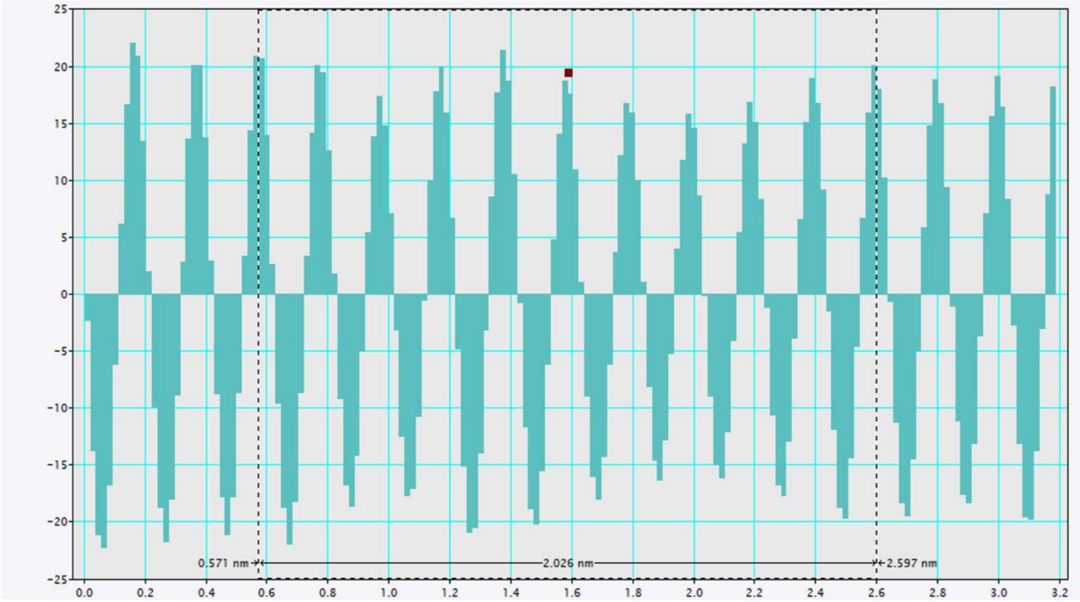

Fig. S4. Line profile of IFFT image. Corresponding to the region marked with a red box in Fig. 1g.

The facet information corresponding to the region marked with a red box in Fig. 1g is provided by the fast Fourier transform (FFT). The (031) planes of cubic Fe_3C are revealed. The inverse fast Fourier transform (IFFT) image of the (031) facet of cubic Fe_3C is also given in Fig. 1h, and the interplanar distance between the adjacent fringes was confirmed to be about 2.026 nm for 10 stacks.

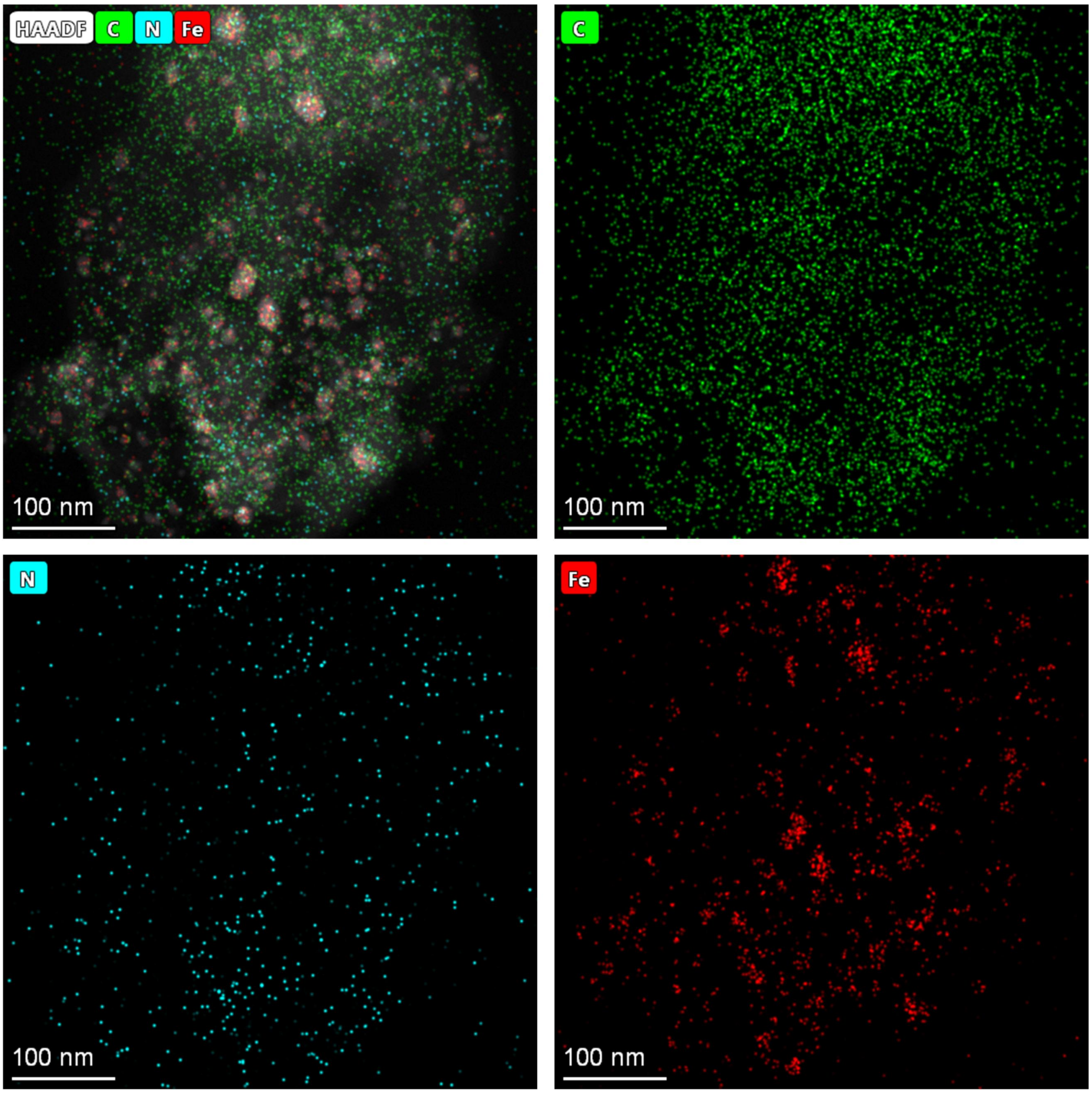

Fig. S5. HAADF-STEM image and EDS mapping. Corresponding to C, N and Fe elements for Fe_3C-NG.

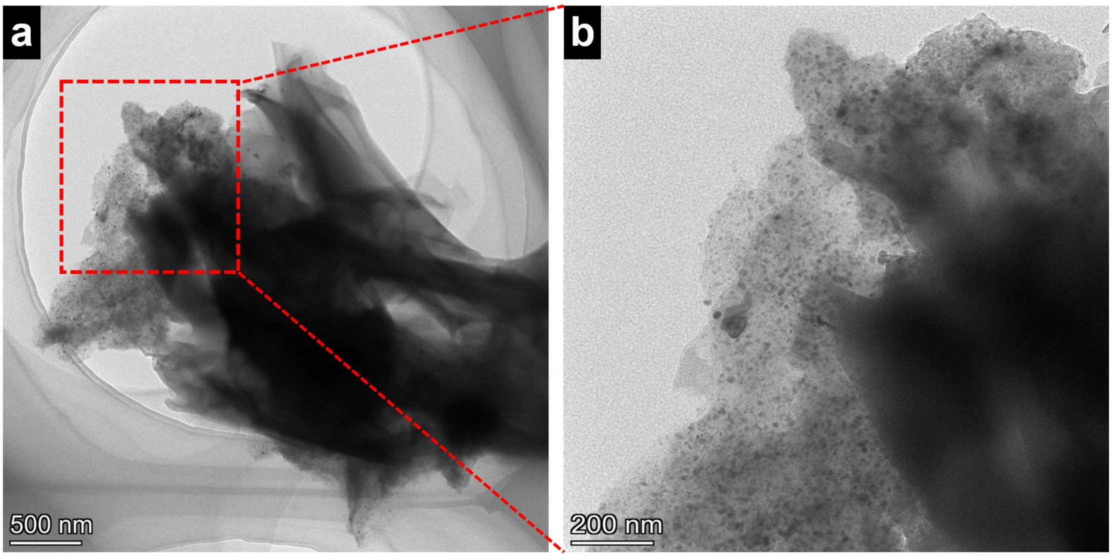

Fig. S6. Structure characterizations of the Fe_3C-NG@NiFe heterojunction catalyst. (a-b) TEM images of Fe_3C-NG@NiFe with different magnifications.

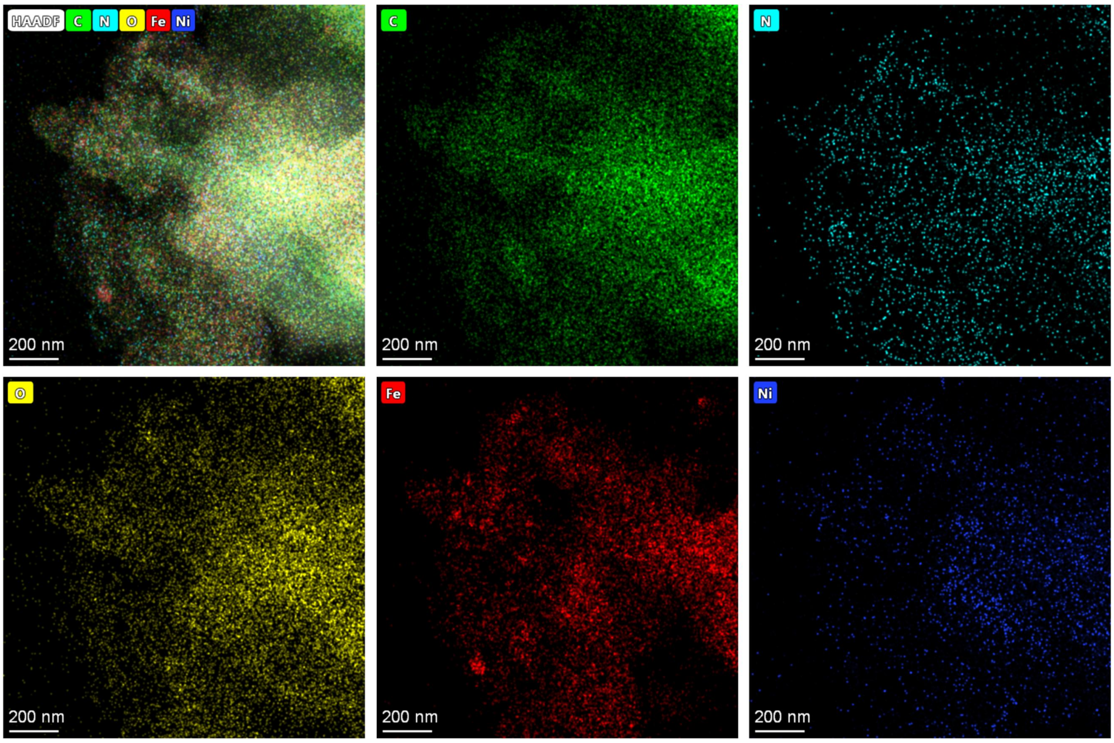

Fig. S7. HAADF-STEM image and EDS mapping. Corresponding to C, N, O, Fe and Ni elements for Fe_3C-NG@NiFe.

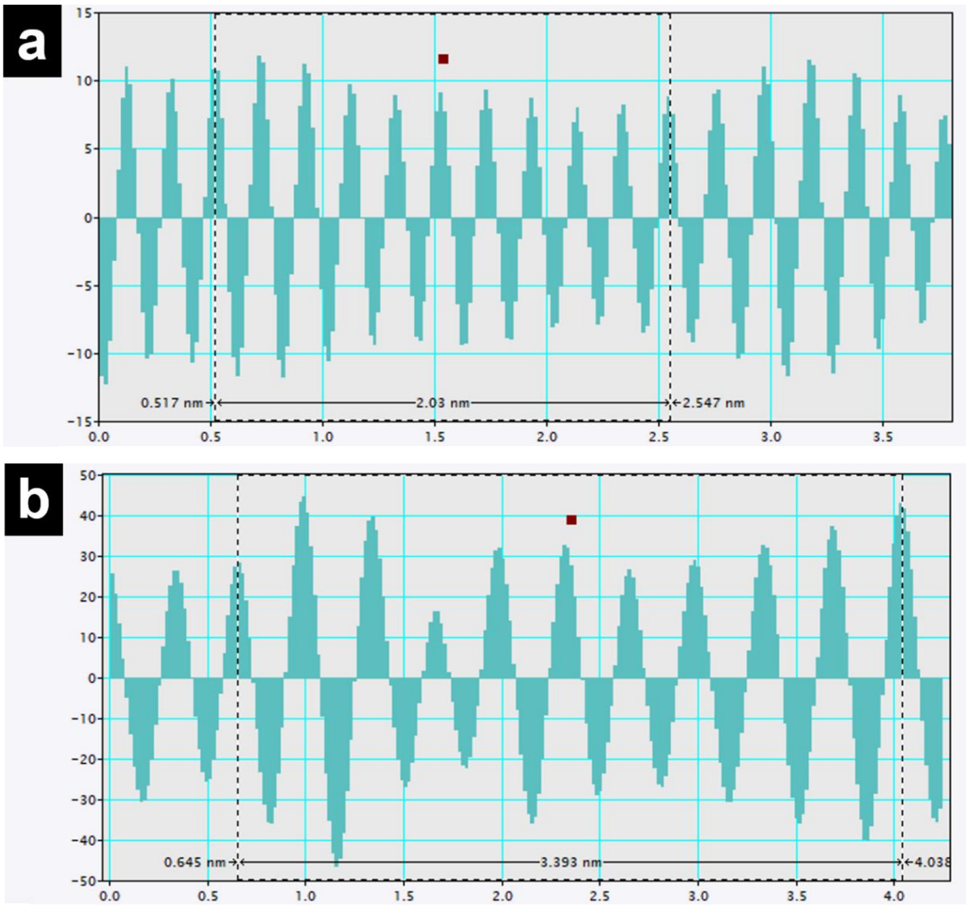

Fig. S8. The line profiles of IFFT images. (a-b) Corresponding to the Fig. 1l and Fig. 1m, respectively.

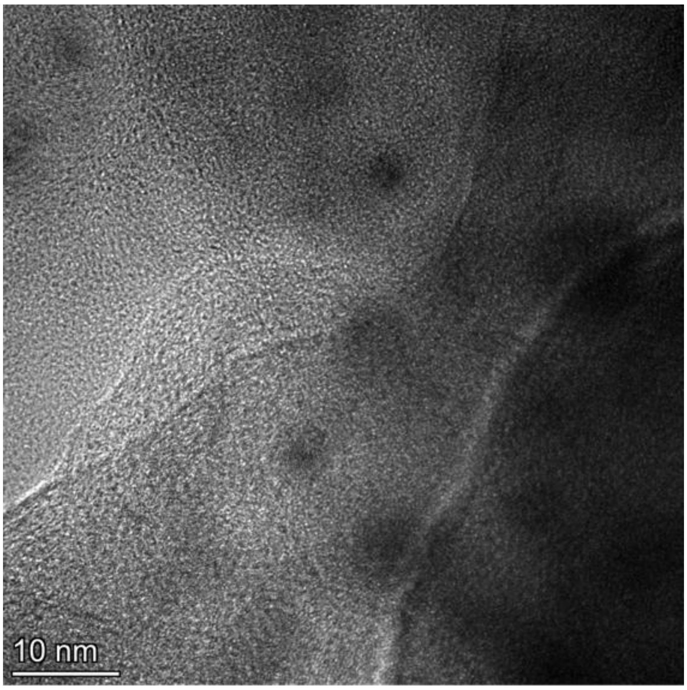

Fig. S9. HRTEM image of Fe_3C-NG@NiFe.

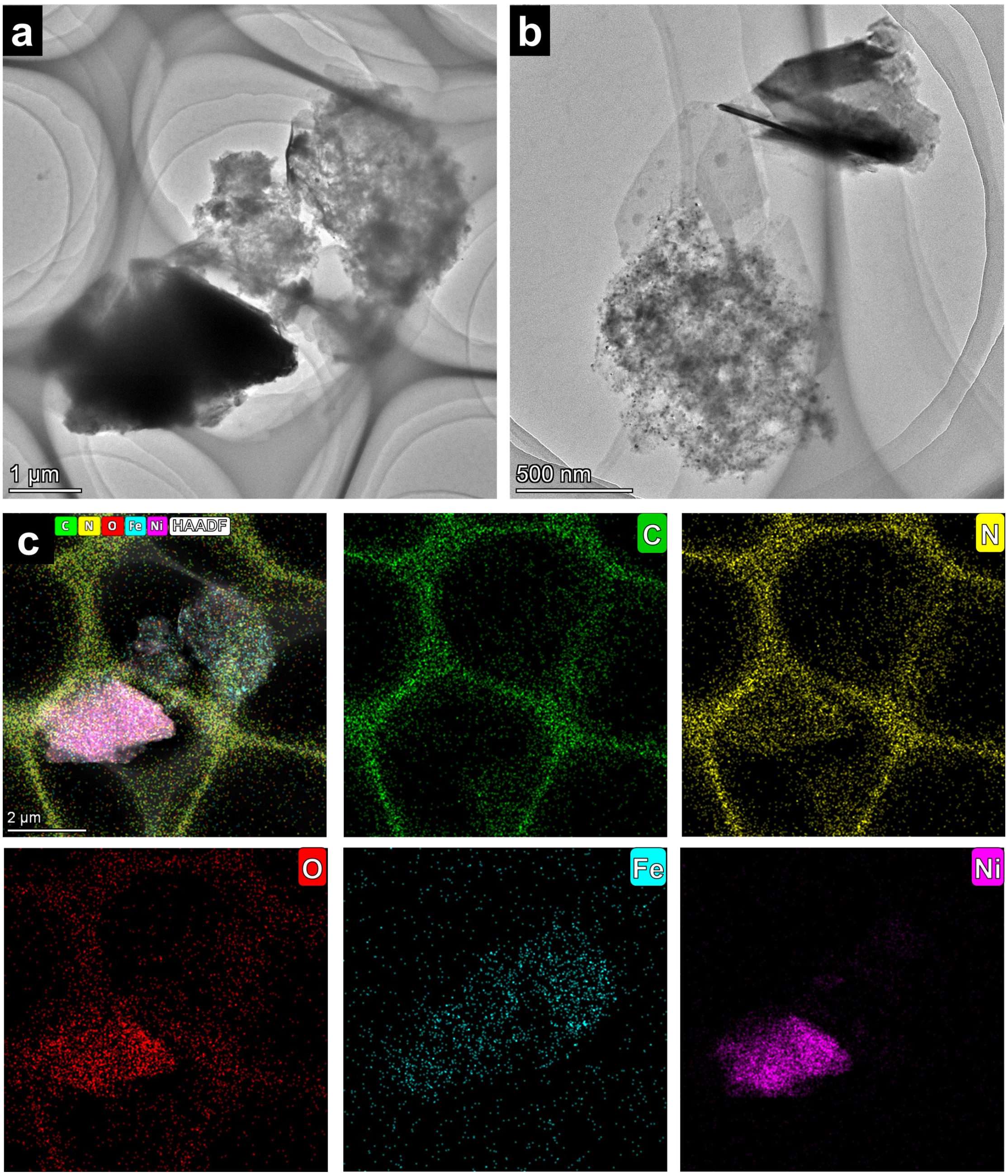

Fig. S10. Structure characterizations of the Fe_3C-NG/NiFe by simply mechanically mixing Fe_3C-NG and NiFe LDH. (a-b) TEM images of Fe_3C-NG/NiFe with different magnifications. (c) HAADF-STEM image and EDS mapping.

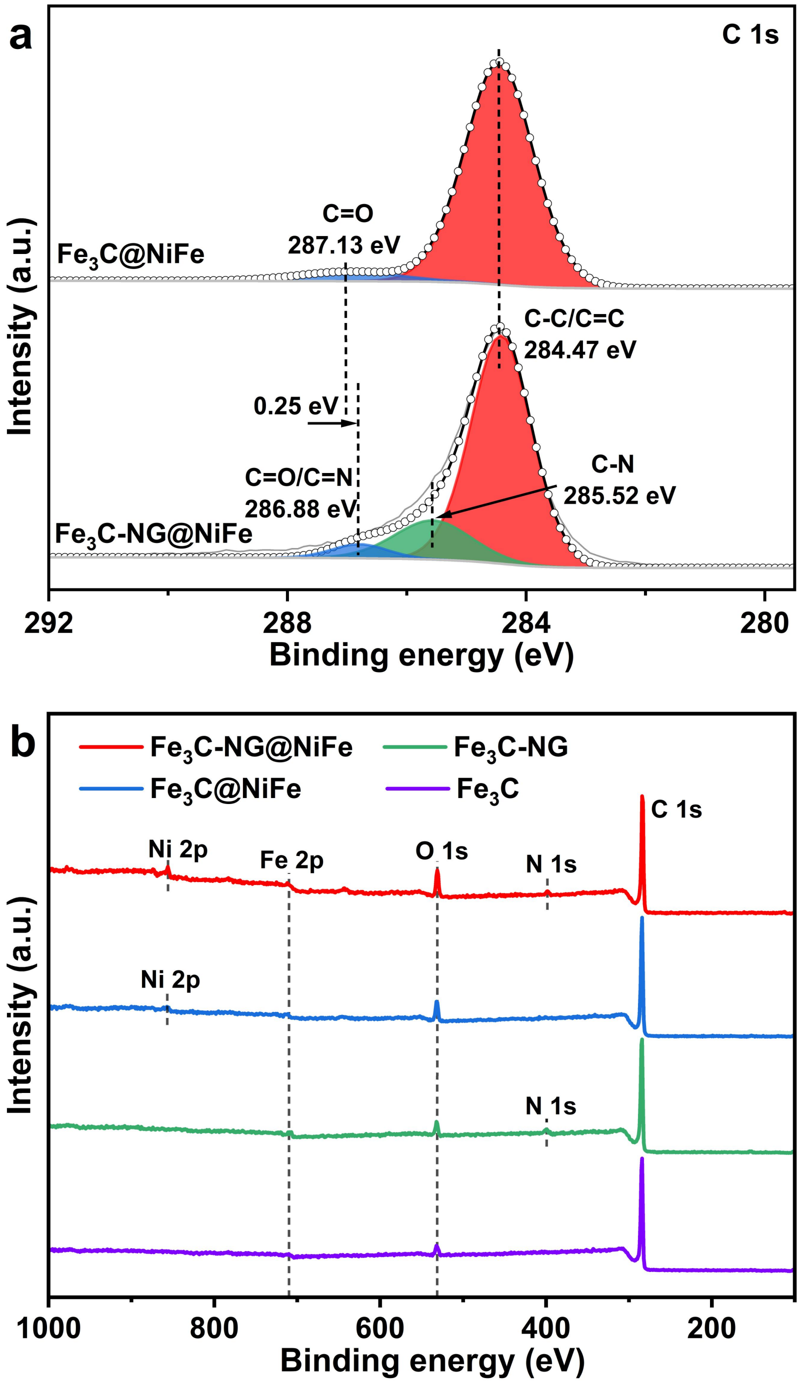

Fig. S11. XPS spectra. (a) High-resolution XPS spectra of C 1s for Fe_3C@NiFe and Fe_3C-NG@NiFe. (b) XPS survey spectra of Fe_3C, Fe_3C-NG, Fe_3C@NiFe, and Fe_3C-NG@NiFe.

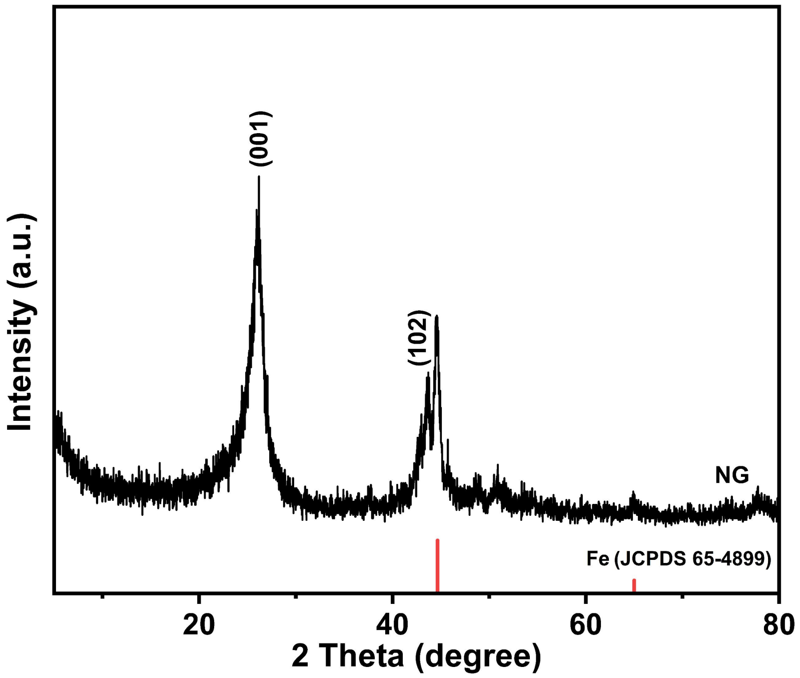

Fig. S12. XRD pattern of prepared NG. Fe_3C in Fe_3C-NG is etched with 5 mol L^{-1} HCl to get almost pure NG.

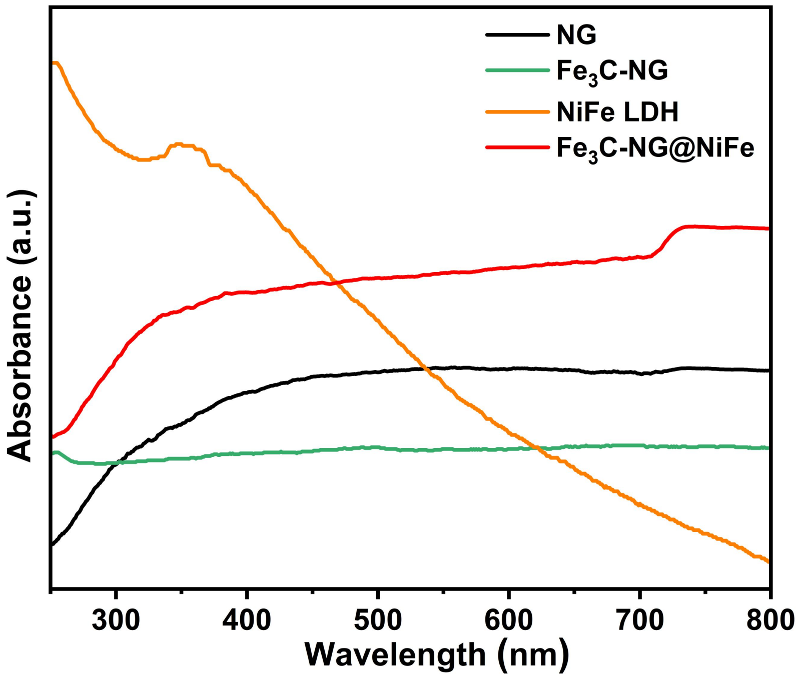

Fig. S13. UV-vis absorbance spectra. NG, Fe_3C-NG, NiFe LDH, and Fe_3C-NG@NiFe.

An energy diagram was constructed based on a series of experimental results to elucidate the formation of p-n heterojunctions and the nature of the synergistic effect between Fe_3C-NG and NiFe LDH. The band-gap energy (E_g) can be estimated from the UV-vis results according to the following Equation S1:

$$(ahv)^n = A\left(hv - E_g\right) \qquad (S1)$$

Where hν denotes incident He (I) energy, which is a constant of 21.2 eV; where α and A are the absorption coefficient and constant, respectively; n (1/2 or 2) depends on the semiconductor type (direct or indirect semiconductor) of material.[1]

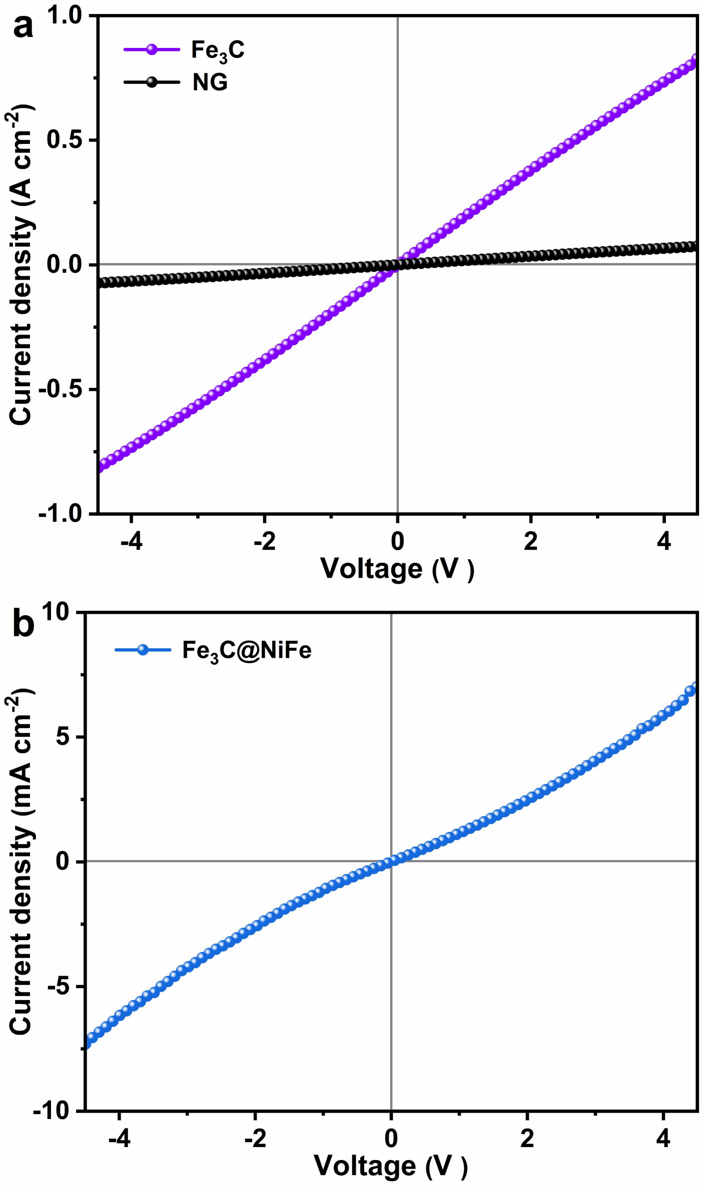

Fig. S14. I-V curves. (a) Fe_3C, NG, and (b) Fe_3C/NiFe LDH were deposited on an FTO substrate with Ag electrodes.

I-V curves of as-designed catalysts

Taking Fe_3C-NG/NiFe LDH heterojunction films device as an example, the Fe_3C-NG/NiFe LDH heterojunction films were deposited on fluorine-tin-oxide (FTO) conductive glass. The spin-coating method was used to deposit Fe_3C-NG and NiFe LDH layers onto the FTO glass at 1500 rpm min^{-1}. The Ag electrode was thermally evaporated using the high vacuum resistance evaporative deposition system under a vacuum pressure of 5×10^{-3} Pa. The current density-voltage (I-V) curves were measured using Keithley 2400 digital source meter over the voltage range from −5.0 to 5.0 V.

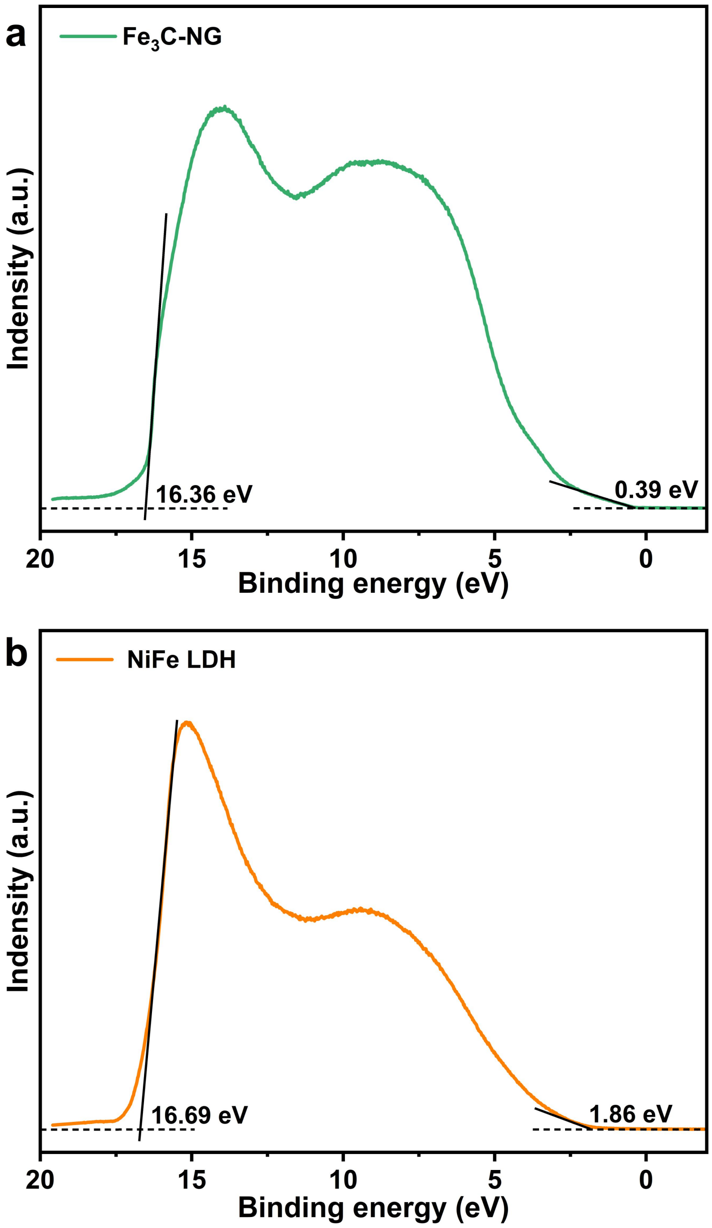

Fig. S15. Ultraviolet photoelectron spectroscopy (UPS). (a) Fe_3C-NG and (b) NiFe LDH.

The value of the work function (W_F) is obtained from UPS results based on the following Equation S2:

$$W_F = hv - \left|E_{cutoff} - {E_F}^0\right| \tag{S2}$$

Where E_{cutoff} is the higher binding energy displayed in energy offsets in UPS raw data, E_F^0 is the Fermi level ($E_F^0 = 0$) of the spectrometer after calibration.[2]

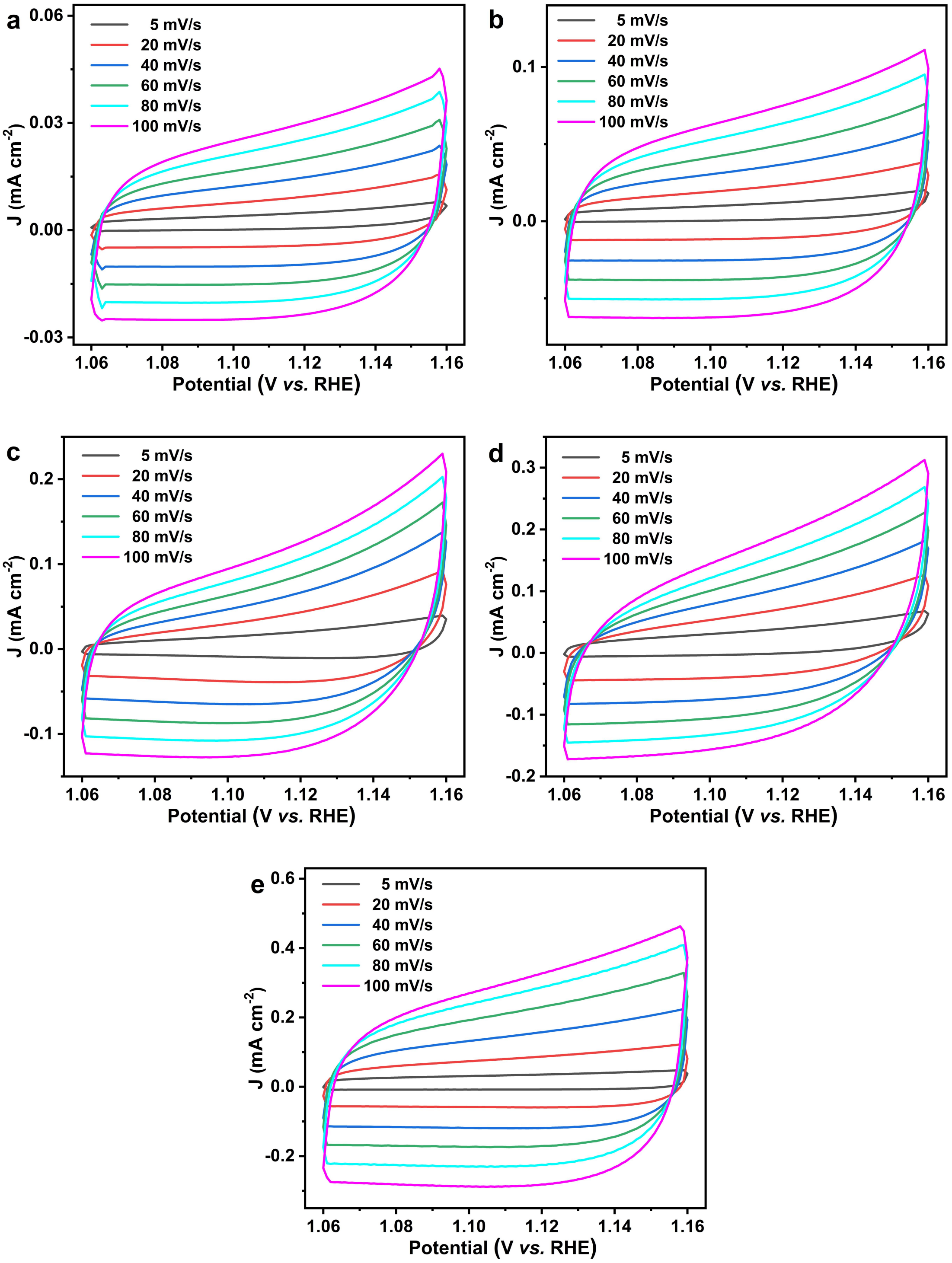

Fig. S16. CV curves at different scan rates. (a) NF, (b) Fe_3C, (c) Fe_3C-NG, (d) Fe_3C@NiFe, and (e) Fe_3C-NG@NiFe in the range from 1.06 V to 1.16 V vs. RHE.

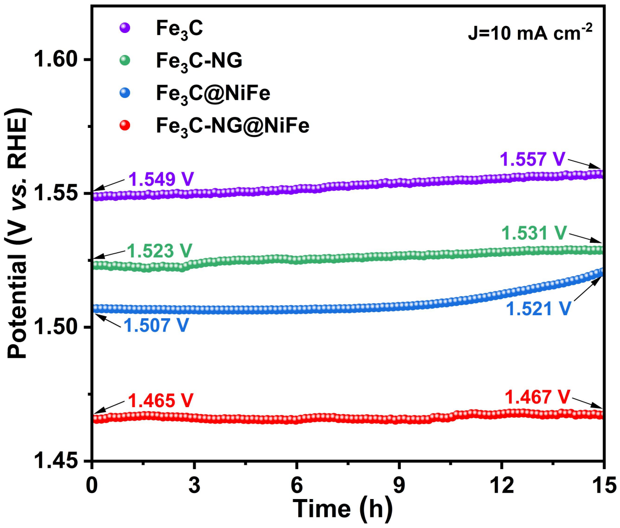

Fig. S17. Chronopotentiometry (CP) curves. Fe$_3$C, Fe$_3$C-NG, Fe$_3$C@NiFe, and Fe$_3$C-NG@NiFe at the constant current density of 10 mA cm^{-2}.

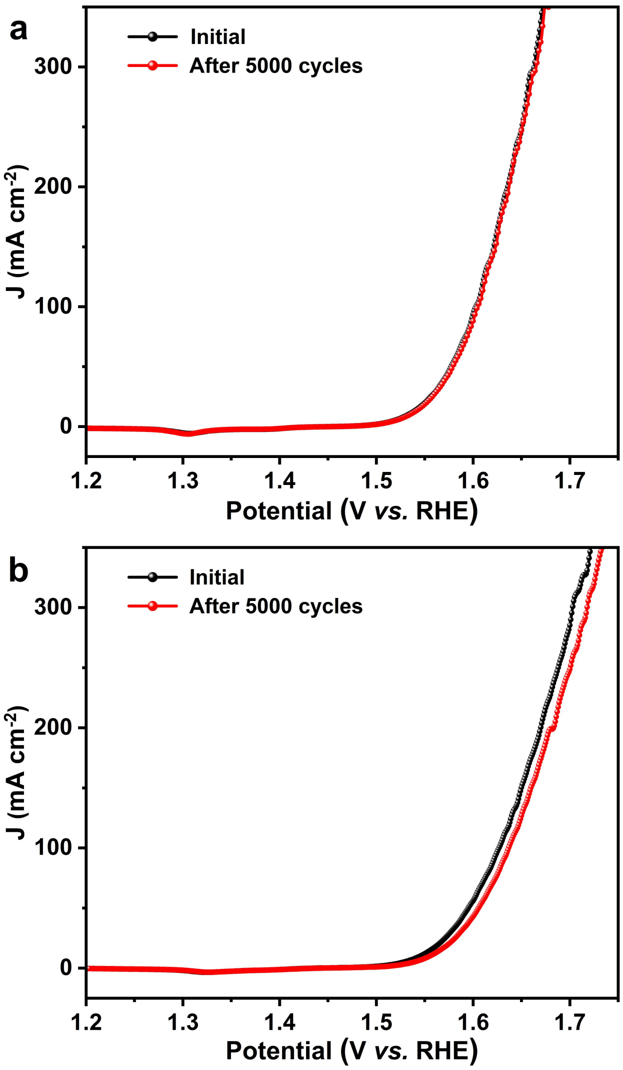

Fig. S18. OER polarization curves. (a) Fe$_3$C-NG and (b) Fe$_3$C before and after 5000 CV cycles.

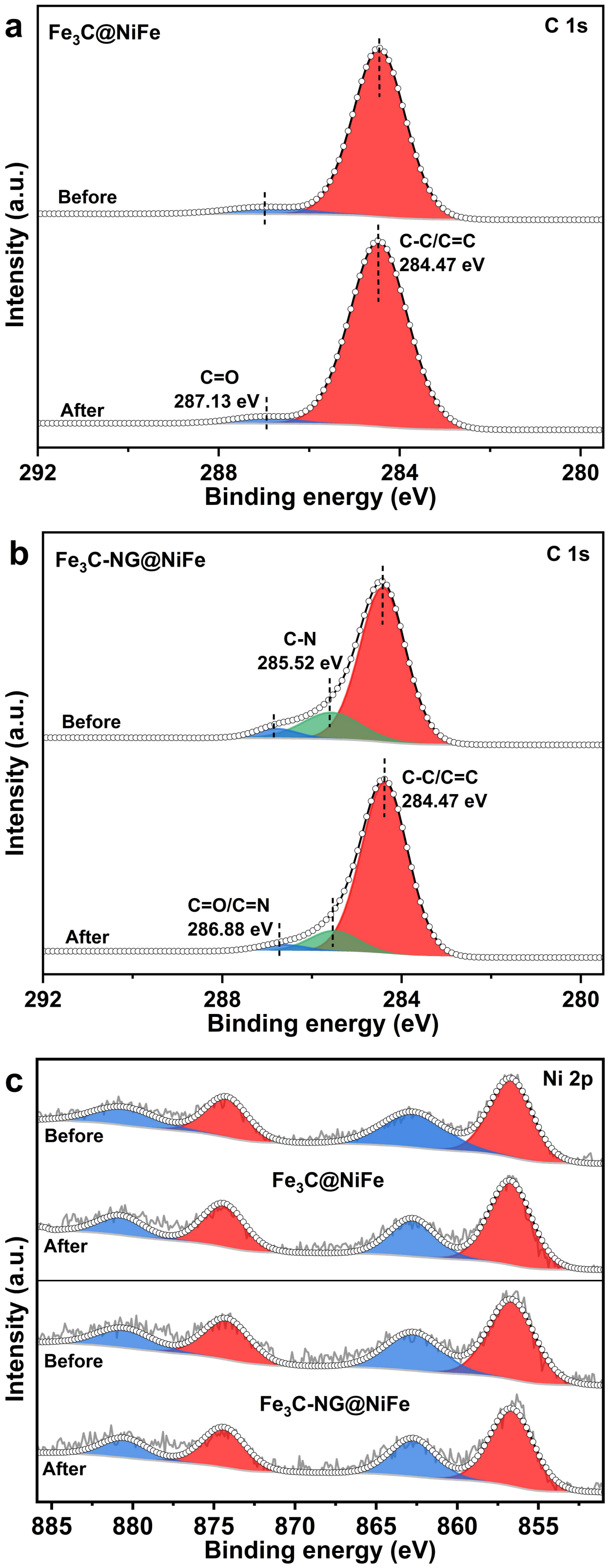

Fig. S19. XPS spectra of Fe_3C@NiFe and Fe_3C-NG@NiFe before and after 5000 CV cycles. The C 1s high-resolution XPS spectra of (a) Fe_3C@NiFe and (b) Fe_3C-NG@NiFe. (c) High-resolution XPS spectra of Ni 2p for Fe_3C@NiFe and Fe_3C-NG@NiFe catalysts.

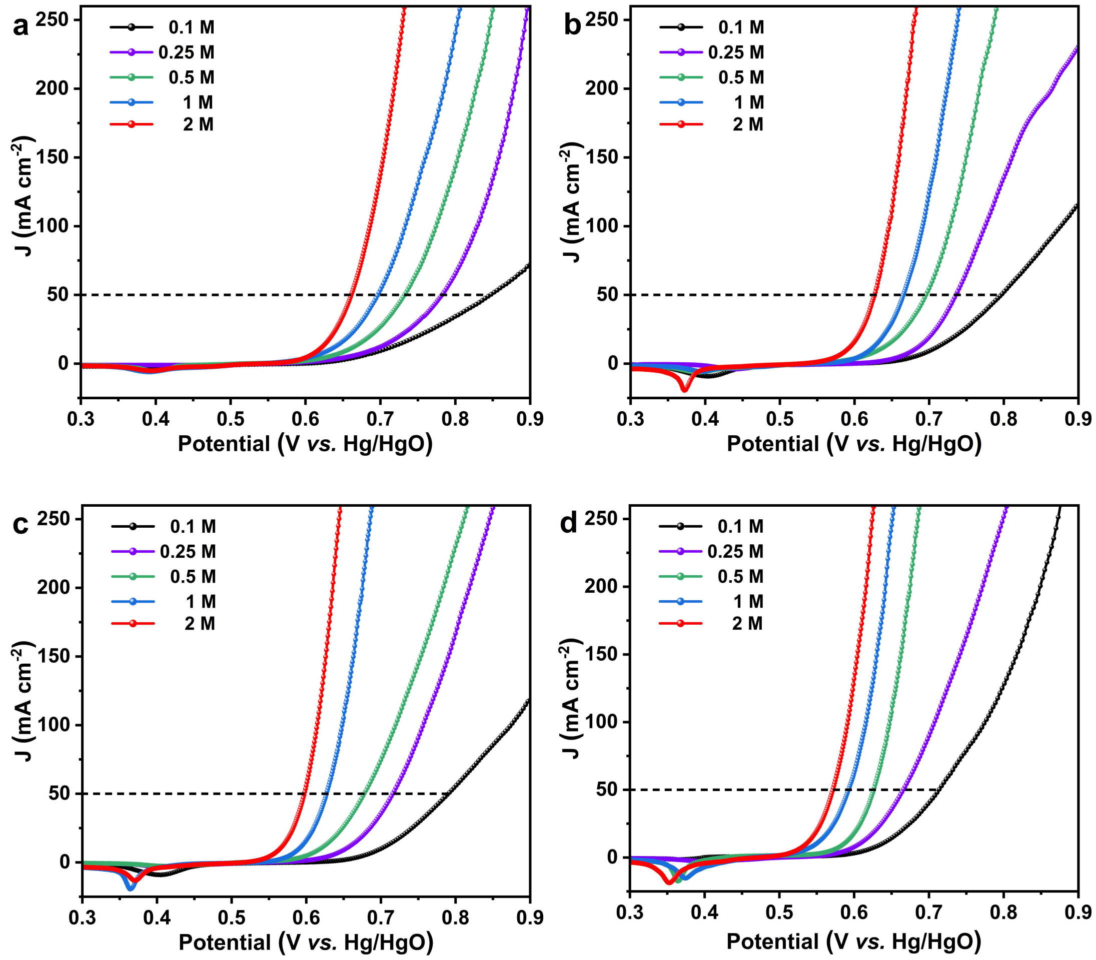

Fig. S20. LSV curves at KOH concentrations of 0.1, 0.25, 0.5, 1, and 2 M. (a) Fe_3C, (b) Fe_3C-NG, (c) Fe_3C@NiFe, and (d) Fe_3C-NG@NiFe.

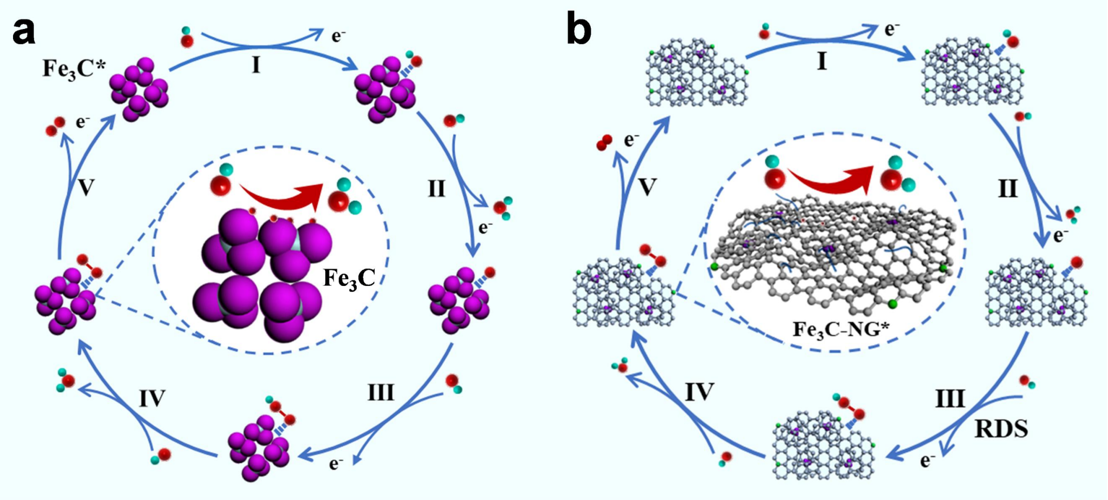

Fig. S21. The reaction mechanism and electron transfer diagram of (a) Fe_3C and (b) Fe_3C-NG in alkaline medium.

Table S1. The C_{dl}, ECSA, and Δn values of OER electrode catalysts.

Catalyst	**NF**	**Fe$_3$C**	**Fe$_3$C-NG**	**Fe$_3$C@NiFe**	**Fe$_3$C-NG@NiFe**
C_{dl} (mF cm^{-2})	0.25	0.64	1.17	1.46	2.93
ECSA (cm^2)	6.25	16	29.25	36.5	73.25
Δn a)	1	2.56	4.68	5.84	11.72

a) The Δn is the ECSA multiple of prepared electrocatalyst to bare NF.

Table S2. Comparison of the OER performance between Fe$_3$C-NG@NiFe and the recently reported heterojunction electrocatalysts in 1 M KOH solution.

Electrocatalysts	**Type**	**Current density (mA cm^{-2})**	***η*** **(mV)**	**Tafel slope (mV dec^{-1})**	**Ref.**
P-CoFe-LDH@MXene	Schottky	200	246	53.2	3
CoFe-LDH@MXene	Schottky	200	330	82	
CoMn/CoMn$_2$O$_4$	Schottky	100	380	68	4
MnCo-CH@NiFe-OH	p-n	100	250	49	2
NiFe-LDH/NiS	Schottky	100	277	60.1	5
FeCoNi-LDH/CuO/Cu	Schottky	50	243	63.8	6
CuO@CoOOH	p-n	20	273	51.7	7
FeNi-LDH/CoP	p-n	20	231	33.5	8
Co$_2$P$_2$O$_7$@N,P-C	Schottky	10	270	49.1	9
Ni/MnO$_2$@CN	Schottky	10	250	48	10
Ni/CeO$_2$@N-CNFs	Schottky	10	230	54.2	11
Co$_2$N$_{0.67}$-BHPC	n-n	10	340	70	12
Co$_2$O$_3$-BHPC	p-n	10	500	99	
Co-BPDC/Co-BDC-3	Schottky	10	335	72.1	13
Co/Co$_2$P@NPCNTs	Schottky	10	310	71.5	14
Co$_2$P/CoP@Co@NCNT	Schottky	10	256	46	15
CeO$_2$/Co$_3$O$_4$	p-n	10	265	68.1	16
NiSe$_2$/FeSe$_2$	p-p	10	256	50	17
NiSe$_2$/CoSe$_2$	p-p	10	304	69	
Fe$_3$C-NG@NiFe	**Schottky + p-n**	**10**	**231**	**41.5**	**This work**

Table S3. Potential of as-prepared catalysts at different KOH concentrations obtain from the current density at 50 mA cm^{-2}.

Electrocatalysts	**Potential at different KOH concentrations (mV vs Hg/HgO)** [a]				
	2 M	**1 M**	**0.5 M**	**0.25 M**	**0.1 M**
Fe_3C	660.7 ± 0.9	697.2 ± 3.6	722.3 ± 1.6	781.5 ± 2.7	846.4 ± 1.4
Fe_3C-NG	624.4 ± 1.5	665.9 ± 0.9	696.2 ± 1.4	730.1 ± 2.1	796.6 ± 2.3
Fe_3C@NiFe	596.8 ± 0.4	627.1 ± 4.1	666.8 ± 2.2	711.1 ± 2.0	789.2 ± 2.1
Fe_3C-NG@NiFe	571.4 ± 1.3	592.8 ± 1.2	625.9 ± 1.7	667 ± 2.4	713.3 ± 1.8

[a] The values are the arithmetic mean from five independent measurements. The errors indicate the standard deviation based on five independent measurements.

The standard deviation (SD) analysis method is used for descripting error bars because it assesses how data points spread out around the mean value. The SD is calculated by Equation S3,

$$SD = \sqrt{\frac{\sum_{i=1}^{n} (X_i - M)^2}{n-1}} \qquad (S3)$$

where X is the individual data points, M is the mean, and Σ (sigma) refers to the summation that finds the sum for all the n data points. Each mean value and error bar was deduced from five independent measurements.

Supplementary Note 1. Evaluation of intrinsic catalytic activity of as-designed OER catalysts

Electrochemically active surface area (ECSA) is an important indicator for OER catalysts, which was obtained indirectly from cyclic voltammetry (CV) curves at a series of scan rates (Fig. S16a-e). [18] In detail, by plotting the ΔJ ($\Delta J = |J_{anodic} - J_{cathodic}|/2$) at 1.11 V vs. RHE (in the Faradaic silence potential range) against the scan rates, the linear slope is obtained, which is a positive correlation with the double-layer capacitance (C_{dl}). The ECSA of electrodes can be calculated from C_{dl} to the equation:

$$ECSA = A\frac{C_{dl}}{C_s} \qquad (S4)$$

Where C_s is the specific capacitance of an automatically smooth planer surface and is considered to be 0.04 mF cm^{-2} in 1 M KOH electrolyte, the C_s value of 1×1 cm^2 depends on the contact area between the catalyst and NF substrate. [19, 20]

To accurately estimate the intrinsic OER activity of the as-prepared electrocatalysts, the electrocatalytic activity of each catalytic site was normalized against ECSA (i.e., the OER current density was converted to J_{ECSA}). The J_{ECSA} was conducted by all the measured LSV current densities being calibrated according to the formula: $J_{ECSA} = J_m/\Delta n$ (measured current density J_m, the multiples of ECSA of as-prepared electrocatalysts against bare NF are expressed as Δn), which can reflect the truest active area.

Supplementary Note 2. Microkinetic analysis of designed OER catalysts

The OER electrokinetic analysis is mainly based on a modified quasi-Langmuir model established by relevant literature, in which the key steps are defined by one pre-equilibrium step (PES) plus four-electron transfer processes. [21, 22] To study the order of hydroxyl ions concentration ([OH⁻]) on the reaction rate, in principle, we can first measure the variation of the potential with changing [OH⁻] in a constant current density (in the Tafel region), then the order of [OH⁻] can be determined by Equation S5: [23, 24]

$$\left(\frac{\partial \log j}{\partial \log [OH^-]}\right)_E = -\frac{\left(\frac{\partial E}{\partial \log [OH^-]}\right)_j}{\left(\frac{\partial E}{\partial \log j}\right)_{pH}} \qquad (S5)$$

In all cases, the initial step(s) should be the oxidation of the active centers accompanied by proton transfers (Equation S6). The Nernst equation (Equation S7) applies in these systems. Here, *x* is the number of protons being transferred, while *y* is the number of electrons being transferred at the same time.

$$Red + xOH^- \rightarrow Ox + xH_2O + ye^- \qquad (S6)$$

$$E = E_0 - \frac{RT}{yF} ln\left(\frac{[Red][OH^-]^x}{[Ox]}\right) \qquad (S7)$$

Notably, the ratio of [*Red*]/[*Ox*] is constant at equilibrium. Therefore, Equation S8 can be rearranged as:

$$E = E_0^{'} - \frac{2.303xRT}{yF} lg([OH^-]) \qquad (S8)$$

The ratio of x/y can be determined by the slope of potential-log [OH⁻] curves.

References

1. N. Zhang, D. Chen, F. Niu, S. Wang, L. Qin and Y. Huang, *Sci. Rep.*, 2016, **6**, 26467.
2. Y. Zeng, Z. Cao, J. Liao, H. Liang, B. Wei, X. Xu, H. Xu, J. Zheng, W. Zhu, L. Cavallo and Z. Wang, *Appl. Catal. B: Environ.*, 2021, **292**, 120160.
3. L. Deng, K. Zhang, D. Shi, S. Liu, D. Xu, Y. Shao, J. Shen, Y. Wu and X. Hao, *Appl. Catal. B: Environ.*, 2021, **299**, 120660.
4. C. Wang, H. Lu, Z. Mao, C. Yan, G. Shen and X. Wang, *Adv. Funct. Mater.*, 2020, **30**, 2000556.
5. Q. Wen, K. Yang, D. Huang, G. Cheng, X. Ai, Y. Liu, J. Fang, H. Li, L. Yu and T. Zhai, *Adv. Energy Mater.*, 2021, **11**, 2102353.
6. Q. Ouyang, S. Cheng, C. Yang and Z. Lei, *J. Mater. Chem. A*, 2022, **10**, 11938-11947.
7. J. Hu, A. Al-Salihy, J. Wang, X. Li, Y. Fu, Z. Li, X. Han, B. Song and P. Xu, *Adv. Sci.*, 2021, **8**, 2103314.
8. K. He, T. Tadesse Tsega, X. Liu, J. Zai, X.-H. Li, X. Liu, W. Li, N. Ali and X. Qian, *Angew. Chem. Int. Ed.*, 2019, **58**, 11903-11909.
9. D. Liang, C. Lian, Q. Xu, M. Liu, H. Liu, H. Jiang and C. Li, *Appl. Catal. B: Environ.*, 2020, **268**, 118417.
10. G. Qian, J. Chen, T. Yu, J. Liu, L. Luo and S. Yin, *Nano-Micro Lett.*, 2021, **14**, 20.
11. T. Li, J. Yin, D. Sun, M. Zhang, H. Pang, L. Xu, Y. Zhang, J. Yang, Y. Tang and J. Xue, *Small*, 2022, **18**, 2106592.
12. X. Lv, Z. Xiao, H. Wang, X. Wang, L. Shan, F. Wang, C. Wei, X. Tang and Y. Chen, *J. Energ. Chem.*, 2021, **54**, 626-638.
13. Q. Zha, F. Yuan, G. Qin and Y. Ni, *Inorg. Chem.*, 2020, **59**, 1295-1305.
14. H. Yang, B. Wang, S. Kou, G. Lu and Z. Liu, *Chem. Eng. J.*, 2021, **425**, 131589.
15. Z. Lu, Y. Cao, J. Xie, J. Hu, K. Wang and D. Jia, *Chem. Eng. J.*, 2022, **430**, 132877.
16. B. Qiu, C. Wang, N. Zhang, L. Cai, Y. Xiong and Y. Chai, *ACS Catal.*, 2019, **9**, 6484-6490.
17. S. Ni, H. Qu, Z. Xu, X. Zhu, H. Xing, L. Wang, J. Yu, H. Liu, C. Chen and L. Yang, *Appl. Catal. B: Environ.*, 2021, **299**, 120638.
18. C. Wei, S. Sun, D. Mandler, X. Wang, S. Z. Qiao and Z. J. Xu, *Chem. Soc. Rev.*, 2019, **48**, 2518-2534.
19. Q. Sun, Y. Li, J. Wang, B. Cao, Y. Yu, C. Zhou, G. Zhang, Z. Wang and C. Zhao, *J. Mater. Chem. A*, 2020, **8**, 21084-21093.
20. Q. Sun, Y. Dong, Z. Wang, S. Yin and C. Zhao, *Small*, 2018, **14**, 1704137.
21. M. E. G. Lyons and M. P. Brandon, *J. Electroanal. Chem.*, 2010, **641**, 119-130.
22. L. Bai, C.-S. Hsu, D. T. L. Alexander, H. M. Chen and X. Hu, *Nat. Energy*, 2021, **6**, 1054-1066.
23. L. Bai, S. Lee and X. Hu, *Angew. Chem. Int. Ed.*, 2021, **60**, 3095-3103.
24. D. K. Bediako, Y. Surendranath and D. G. Nocera, *J. Am. Chem. Soc.*, 2013, **135**, 3662-3674.